

# Two-Temperature Plasma Modeling of Nitrogen/Hydrogen Arcjets

Thomas W. Megli,\* Herman Krier,† Rodney L. Burton,‡ and Ayhan Mertogul§  
University of Illinois at Urbana–Champaign, Urbana, Illinois 61801

A two-temperature chemical equilibrium model is presented for nitrogen/hydrogen arcjet thrusters. The model is fully viscous and assumes steady, laminar, continuum, axisymmetric flow. A seven-species nitrogen/hydrogen plasma composition of molecules, atoms, ions, and electrons is assumed, and separate energy equations are formulated for the electrons and heavy species. The anode temperature distribution is included, and propellant electrical conductivity is coupled to the plasma properties, allowing for a self-consistent current distribution. The numerical solution employs the compressible form of the pressure-implicit with splitting of operators algorithm to solve the continuity and momentum equations. Numerical results are presented for a low-power thruster with simulated hydrazine propellant. The centerline constrictor region of the arcjet flowfield is predicted to be near thermal equilibrium, while a high degree of thermal nonequilibrium is predicted in the near-anode and downstream regions of the arcjet nozzle. Strong electric fields near the anode produce elevated electron temperatures that enhance ionization levels and electrical conduction through the arcjet boundary layer. Thus, the two-temperature approach is required to model the plasma current distribution accurately.

## Nomenclature

$C$	= coulomb charge
$c_i$	= mean thermal speed of species $i$ , m/s
$D_i$	= effective diffusion coefficient of species $i$ , m <sup>2</sup> /s
$d$	= diameter, m
elst	= elastic energy transfer, W/m <sup>3</sup>
$g_0$	= gravitational acceleration at sea level, m/s <sup>2</sup>
$H$	= heavy species total particle energy, J
$h$	= Planck's constant, J-s
$h_i$	= enthalpy of species $i$ , J/kg
$I$	= integrated total current, A
$I_{sp}$	= specific impulse, s
$j$	= current density, A/m <sup>2</sup>
$k_b$	= Boltzmann's constant, J/K
$k_c$	= Coulomb constant, Nm <sup>2</sup> /C <sup>2</sup>
$M$	= Mach number
$\dot{m}$	= mass flow rate, kg/s
$m_i$	= mass of species $i$ , kg
$m_{ij}$	= reduced mass, kg
$n_i$	= number density of species $i$ , m <sup>-3</sup>
$P$	= electrical power, W
$p$	= pressure, N/m <sup>2</sup>
$Q_{ij}$	= collision cross section, m <sup>2</sup>
$T$	= thrust, N
$T_a$	= anode temperature, K
$T_c$	= cathode temperature, K
$T_e$	= electron temperature, K
$T_g$	= heavy species temperature, K
$u$	= axial velocity, m/s
$V$	= voltage, V

$v$	= radial velocity, m/s
$\mathbf{v}$	= velocity vector, m/s
$w$	= azimuthal swirl velocity, m/s
$x_i$	= mole fraction of species $i$
$x_{mol}$	= mixture parameter in $x_{mol}N_2 + H_2$
$x, r, \theta$	= cylindrical coordinates
$y_{e,i}$	= mass fraction of species $i$
$Z_i$	= thermodynamic partition functions
$\delta$	= electron–molecule inelastic loss factor
$\epsilon$	= anode emissivity
$\epsilon_d$	= dissociation energy, J
$\epsilon_i$	= ionization energy, J
$\theta_{vH_2}$	= H <sub>2</sub> vibrational temperature, K
$\theta_{vN_2}$	= N <sub>2</sub> vibrational temperature, K
$\Lambda_e$	= coulomb logarithm term
$\lambda_a$	= anode thermal conductivity, W/m-K
$\lambda_e$	= electron thermal conductivity, W/m-K
$\lambda_h$	= heavy species thermal conductivity, W/m-K
$\mu$	= gas viscosity, kg/m-s
$\nu$	= collision frequency, s <sup>-1</sup>
$\rho$	= mass density, kg/m <sup>3</sup>
$\sigma$	= electrical conductivity, $\Omega\cdot m^{-1}$
$\tau$	= stress tensor, N/m <sup>2</sup>
$\bar{\Omega}_{ij}$	= collision integral, m <sup>2</sup>

## Introduction

THE arcjet is shown schematically in Fig. 1. Injected mass flow  $\dot{m}$  enters the constrictor, and is ionized and heated by current flowing from anode to cathode. The fluid dynamics and energy transfer within the arcjet thruster are nonlinear and strongly coupled. The propellant, typically injected upstream of the constrictor, is given an azimuthal (or swirl) velocity component. Propellant heating occurs in the arc discharge, produced by a voltage difference between the anode thruster nozzle and a conical cathode on the upstream side of the constrictor. Typical operating voltages for 1-kW class arcjets are 100-V dc at a current of  $I = 10$  A. The arc current distribution depends on several factors in addition to the geometry. The distribution is coupled to the propellant mass flow rate, composition, thermal properties, electrical conductivity, and gas-dynamic properties.<sup>1</sup>

Both chemical and thermal processes in the arcjet are characterized as nonequilibrium. Arc current is converted to elec-

Received Nov. 2, 1994; revision received Nov. 8, 1995; accepted for publication Aug. 17, 1996. Copyright © 1996 by the American Institute of Aeronautics and Astronautics, Inc. All rights reserved.

\*Ph.D. Candidate, Department of Mechanical and Industrial Engineering; currently at Ford Research and Engineering Center, 21500 Oakwood Boulevard, Dearborn, MI 48121. Member AIAA.

†Professor, Department of Mechanical and Industrial Engineering, 1206 West Green Street. Fellow AIAA.

‡Associate Professor, Department of Aeronautical and Astronautical Engineering, 104 South Wright Street. Associate Fellow AIAA.

§Postdoctoral Research Associate, Department of Mechanical and Industrial Engineering, 1206 West Green Street. Member AIAA.

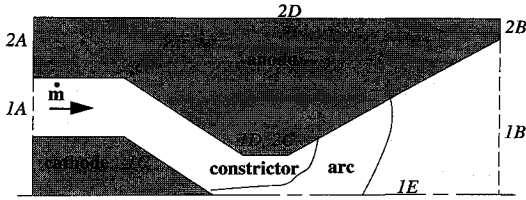


Fig. 1 Schematic of arcjet thruster indicating fluid and anode domain boundaries.

tron thermal energy through ohmic dissipation. The electrons transfer thermal energy to heavy species in the arc plasma through collisions. This energy is then converted to thrust as the fluid accelerates through the nozzle. In regions of low pressure and/or elevated ohmic heating, collisional coupling between electrons and heavy species may not establish equal gas and electron temperatures. Additionally, flow velocities are large so that fluid residence times in the nozzle are of the order of a few  $\mu$ s, and much of the energy invested in dissociation and ionization is frozen. Pressures drop from roughly 1 atm at the constrictor to millitorr conditions at the exit; radial diffusion of electrons from the arc core is important in determining the arc structure.

The thrust and specific impulse produced by an arcjet are determined by several factors, including the power transferred to the propellant, the extent of both thermal and chemical nonequilibrium, the propellant gas mixture, and the arcjet nozzle geometry. Other factors that contribute to the overall performance include the thermal loading of the anode,<sup>2</sup> and the voltage sheaths at the electrodes. A comprehensive model of an arcjet thruster is highly complex, including plasmadynamic, fluid dynamic, radiative, and surface and volumetric heat transfer phenomena.

Most arcjet design strategies to date have been empirical, with design improvements based on experimental observations. The need for a more complete description of the complex physical processes has resulted in a variety of numerical efforts ranging from simplified one-dimensional models<sup>3-8</sup> to more comprehensive two-dimensional descriptions of the gas-dynamics and energy transfer processes.<sup>9-22</sup> Comprehensive arcjet models are required to 1) interpret experimental results, 2) understand the physical processes in regions of the thruster where diagnostic techniques are challenging, 3) improve arcjet performance, and 4) scale the devices to higher specific power levels.

## Model

An axisymmetric, steady, laminar, continuum, viscous flow, two-temperature thermal nonequilibrium model is formulated for a direct current arcjet with flow swirl, a variable nozzle geometry, and a variable mixture ratio of nitrogen and hydrogen. Flow swirl is modeled by including an azimuthal momentum equation. The model predicts thrust, specific impulse, and internal fields for  $p$ ,  $\rho$ ,  $n_i$ , and  $T_a$ ,  $T_e$ , and  $T_g$ . Additionally, the model predicts the distributions of  $j$ ,  $V$ , and  $u$ ,  $v$ , and  $w$ . Chemical equilibrium is assumed; species populations are determined using a generalized law of mass action, species conservation, a plasma equation of state, and charge neutrality.

The details of the model are presented in six sections as 1) fluid dynamic equations, 2) energy equations, 3) electromagnetic equations, 4) species number density equations, 5) transport coefficients, and 6) boundary conditions. The arcjet geometry is described as  $(x, r, \theta)$  for the axial, radial, and azimuthal coordinates, respectively.

## Fluid Dynamic Equations

The viscous fluid dynamic equations are summarized next:

Axial momentum:

$$\frac{\partial(\rho u)}{\partial x} + \frac{1}{r} \frac{\partial(r \rho u v)}{\partial r} = \frac{4}{3} \frac{\partial}{\partial x} \left( \mu \frac{\partial u}{\partial x} \right) + \frac{1}{r} \frac{\partial}{\partial r} \left( \mu r \frac{\partial u}{\partial r} \right) - \frac{2}{3} \frac{\partial}{\partial x} \left( \mu \frac{\partial v}{\partial r} \right) - \frac{2}{3r} \frac{\partial(\mu v)}{\partial x} + \frac{1}{r} \frac{\partial}{\partial r} \left( \mu r \frac{\partial v}{\partial x} \right) - \frac{\partial p}{\partial x} \quad (1)$$

Radial momentum:

$$\frac{\partial(\rho u v)}{\partial x} + \frac{1}{r} \frac{\partial(r \rho v v)}{\partial r} = \frac{\partial}{\partial x} \left( \mu \frac{\partial v}{\partial x} \right) + \frac{4}{3r} \frac{\partial}{\partial r} \left( \mu r \frac{\partial v}{\partial r} \right) + \frac{\partial}{\partial x} \left( \mu \frac{\partial u}{\partial r} \right) + \frac{2\mu}{3r} \frac{\partial u}{\partial x} - \frac{2v}{3r} \frac{\partial \mu}{\partial r} - \frac{4}{3} \frac{\mu v}{r^2} - \frac{2}{3r} \frac{\partial}{\partial r} \left( \mu r \frac{\partial u}{\partial x} \right) - \frac{\partial p}{\partial r} + \frac{\rho w^2}{r} \quad (2)$$

Azimuthal momentum ( $\partial p / \partial \theta = 0$ ):

$$\frac{\partial[\rho u(wr)]}{\partial x} + \frac{1}{r} \frac{\partial}{\partial r} [(r \rho v + 2\mu)(wr)] = \frac{\partial}{\partial x} \left[ \mu \frac{\partial(wr)}{\partial x} \right] + \frac{1}{r} \frac{\partial}{\partial r} \left[ \mu r \frac{\partial(wr)}{\partial r} \right] \quad (3)$$

Axisymmetric continuity:

$$\frac{\partial}{\partial x} (\rho u) + \frac{1}{r} \frac{\partial}{\partial r} (r \rho v) = 0 \quad (4)$$

## Energy Equations

The assumption of thermal nonequilibrium requires separate energy equations for the electrons and heavy species. The electron energy equation is

$$\nabla \cdot \{ [n_e v - (j/e)] (C_{pe} T_e) \} = \nabla \cdot (\lambda_e \nabla T_e) + \nabla \cdot [(1/m_e) \rho C_{pe} T_e D_e \nabla y_e] + [(j \cdot j)/\sigma] - \text{elst} - \text{radiation} \quad (5)$$

where elst represents energy lost through elastic collisions with the heavy species,<sup>23</sup> and radiation denotes optically thin radiation loss because of continuum bremsstrahlung.<sup>24</sup> The elastic energy transfer source term is calculated as the sum of electron-molecule, -atom, and -ion contributions as

$$\text{elst} = 3k_b(T_e - T_g) m_e n_e \sum_{i \neq e} \frac{\delta_{ei} \bar{v}_{ei}}{m_i} \quad (6)$$

where the average collision frequencies  $\bar{v}_{ei}$  between electrons and heavy species are calculated using the mean electron thermal speed and collision cross sections  $Q_{es}$  as<sup>24</sup>

$$\bar{v}_{ei} = \sqrt{8k_b T_e / \pi m_e} n_i Q_{ei} \quad (7)$$

where the electron-single ion cross sections are

$$Q_{e-\text{ion}} = \frac{\pi e^4 k_c^2 \ell_n \Lambda_e}{2(k_b T_e)^2} \quad (8)$$

In Eq. (6), electron-particle collision frequencies are multiplied by the energy loss factor  $\delta_{ei}$  to account for inelastic losses to internal modes.<sup>8,25</sup> Although this energy loss is generally electron temperature-dependent, a constant loss factor of  $\delta = 1$  for neutral and ion collisions and  $\delta = 3000$  for molecular collisions, is employed. The relatively high and energy-independent value of  $\delta$  is chosen because of the following:

- 1) Significant uncertainties in  $\delta$  are noted in the literature.<sup>8</sup>

2) Reasonable predictions for convective effects result, with the arc being swept further downstream as the mass flow rate is increased, as was originally postulated in Ref. 8.

3) Better agreement is achieved between the predicted and experimentally observed operating voltage, while maintaining the equipotential anode voltage boundary condition in the constrictor. This point is further discussed in Refs. 26 and 27.

The energy equation for heavy species (molecules, atoms, and ions) is

$$\nabla \cdot (n_h \mathbf{v} H) = \nabla \cdot (\lambda_h \nabla T_g) + \sum_{i \neq e} \frac{1}{m_i} \nabla \cdot (\rho (C_{pi} T_g + h_i^0) D_i \nabla y_i) + \text{elst} + \nabla \cdot (\mathbf{v} \cdot \boldsymbol{\tau}) \quad (9)$$

where

$$H = \frac{1}{n_h} \sum_{i \neq e} \left[ n_i \left( C_{pi} T_g + h_i^0 + \frac{m_i \mathbf{v} \cdot \mathbf{v}}{2} \right) \right] \quad (10)$$

The ionization and dissociation energies of molecules and atoms are arbitrarily included in the heavy species energy equation as reference enthalpies  $h_i^0$ . The reference enthalpies and specific heats are summarized in Table 1.

The anode temperature distribution is determined from the energy equation for heat conduction in a solid. Neglecting ohmic dissipation in the anode gives

$$\nabla \cdot (\lambda_a \nabla T_a) = 0 \quad (11)$$

where  $\lambda_a = \lambda_a(T_a)$  (as per Ref. 28).

### Species Equations

Assuming chemical equilibrium, the species number densities are given as a function of  $p$ ,  $T_g$ , and  $T_e$ . A seven-species plasma composition of  $N_2$ ,  $H_2$ ,  $N$ ,  $H$ ,  $N^+$ ,  $H^+$ , and electrons is assumed. Dissociation and ionization equations are constructed from a generalized law of mass action as given by entropy maximization.<sup>29</sup> This yields the following equations for the nitrogen and hydrogen species:

$$\frac{n_H^2}{n_{H_2}} = \exp \left( \frac{-\varepsilon_{d,H_2}}{k_b T_g} \right) \left( \frac{\pi m_H k_b T_g}{h^2} \right)^{3/2} \left( \frac{Z_{H,ex}^2}{Z_{H_2,ex} Z_{H_2,rot} Z_{H_2,vib}} \right) \quad (12a)$$

$$\frac{n_N^2}{n_{N_2}} = \exp \left( \frac{-\varepsilon_{d,N_2}}{k_b T_g} \right) \left( \frac{\pi m_N k_b T_g}{h^2} \right)^{3/2} \left( \frac{Z_{N,ex}^2}{Z_{N_2,ex} Z_{N_2,rot} Z_{N_2,vib}} \right) \quad (12b)$$

$$\frac{n_e n_{H^+}}{n_H} = 2 \exp \left( \frac{-\varepsilon_{i,H}}{k_b T_e} \right) \left( \frac{2 \pi m_e k_b T_e}{h^2} \right)^{3/2} \left( \frac{Z_{H^+,ex}}{Z_{H,ex}} \right) \quad (12c)$$

$$\frac{n_e n_{N^+}}{n_N} = 2 \exp \left( \frac{-\varepsilon_{i,N}}{k_b T_e} \right) \left( \frac{2 \pi m_e k_b T_e}{h^2} \right)^{3/2} \left( \frac{Z_{N^+,ex}}{Z_{N,ex}} \right) \quad (12d)$$

In the previous expressions, the excitation partition functions  $Z_{ex}$  are functions of  $T_e$ , whereas  $Z_{rot}$  and  $Z_{vib}$  are functions of  $T_g$ . Note that the ionization levels are largely controlled by  $T_e$ , as indicated by the well-known Saha Eqs. (12c) and (12d),

Table 1 Species reference enthalpies and specific heats

Species	$C_{pi}$ , J/K	$h_i^0$ , J/particle
e	$\frac{5}{2} k_b$	0
$H_2$	$k_b \left\{ \frac{7}{2} + (\theta_{v,H_2}/T_g) [\exp(\theta_{v,H_2}/T_g - 1)^{-1}] \right\}$	$k_b/2 \theta_{v,H_2}$
$N_2$	$k_b \left\{ \frac{7}{2} + (\theta_{v,N_2}/T_g) [\exp(\theta_{v,N_2}/T_g - 1)^{-1}] \right\}$	$k_b/2 \theta_{v,N_2}$
H	$\frac{5}{2} k_b$	$\frac{1}{2} \varepsilon_{d,H_2}$
N	$\frac{5}{2} k_b$	$\frac{1}{2} \varepsilon_{d,N_2}$
$H^+$	$\frac{5}{2} k_b$	$\frac{1}{2} \varepsilon_{d,H_2} + \varepsilon_{i,H}$
$N^+$	$\frac{5}{2} k_b$	$\frac{1}{2} \varepsilon_{d,N_2} + \varepsilon_{i,N}$

which are exclusive functions of  $T_e$ . This choice is justified since ionization is primarily a result of electron-impact processes. Details for the calculation of the various partition functions can be found in Refs. 24 and 29–32.

The plasma equation of state, quasineutrality, and the definition of the mixture parameter  $x_{mol}$  provide the additional relations required to solve for the seven unknown species. Note that the initial mixture composition is written as  $x_{mol} N_2 + H_2$  to that pure hydrogen ( $x_{mol} = 0$ ), simulated hydrazine ( $x_{mol} = \frac{1}{2}$ ), and simulated ammonia ( $x_{mol} = \frac{1}{3}$ ), can be easily investigated:

$$x_{mol} = \frac{2n_{N_2} + n_N + n_{N^+}}{2n_{H_2} + n_H + n_{H^+}} \quad (13)$$

$$n_e = n_{H^+} + n_{N^+} \quad (14)$$

$$p = n_e k_b T_e + (n_{N_2} + n_{H_2} + n_N + n_H + n_e) k_b T_g \quad (15)$$

### Electromagnetic Equations

The calculation of the electrical current distribution is critical to understanding arc physics and poses a challenging problem in arcjet analysis. The current distribution is largely determined by the flowfield  $\sigma$ , which is a strong function of the electron number density and temperature distribution. Numerical arcjet models that assume local thermodynamic equilibrium (LTE) must artificially elevate  $\sigma$  in the cool boundary-layer region to avoid excessive voltage drops near the anode.<sup>11,15</sup> The artificial restriction that  $T_e = T_g$  results in an underprediction for the ionization (and, therefore, electron number density and  $\sigma$ ) in the boundary-layer regions, and a subsequent overprediction in power deposition. Hence, the conductivity floor is employed elsewhere<sup>10,14</sup> to provide agreement between the experimentally observed and predicted power depositions.

Diffusion of electrons from the arc core toward the anode wall also elevates the electron number density and plays an important role in determining the boundary-layer electrical conductivity. This has been demonstrated by Butler et al.,<sup>11</sup> who show that the incorporation of mass diffusion provides a reasonable current distribution without imposing artificial restrictions on  $\sigma$  or the current attachment region. However, the two-temperature solutions of Miller and Martinez-Sanchez<sup>16</sup> and Keefer et al.<sup>17</sup> demonstrate that significant thermal nonequilibrium with elevated  $T_e$  exists outside of the arc core in the constrictor region. These results indicate that both diffusion and increased ionization caused by elevated  $T_e$  are important factors that determine the boundary-layer electrical conductivity. Thus, although both thermal and chemical nonequilibrium effects are significant, this investigation focuses on the thermal nonequilibrium aspects of hydrazine arcjet flows.

The correct approach to the arc anode attachment problem is to model the anode as an equipotential surface and allow the current distribution to be a model output, independent of artificial restrictions. This is a self-consistent approach to solving for the current distribution and electric field simultaneously, for which the current distribution is properly coupled to the flowfield.

Assuming induced magnetic fields are negligible, and neglecting electron pressure gradient driving terms, Ohm's law and current conservation are used to solve for  $j$  and  $V$ .<sup>25</sup> We note that the electron pressure gradient term was included in the model of Miller and Martinez-Sanchez,<sup>16</sup> which treated hydrogen arcjets. Thus

$$-\nabla V = j/\sigma \quad (16)$$

$$\nabla \cdot j = 0 \quad (17)$$

### Transport Coefficients

Transport coefficients are calculated using mean-free-path mixture rules.<sup>33</sup> The viscosity is computed as

$$\mu = \sum_{i=1}^N \left( n_i / \sum_{j=1}^N n_j M_{ij} \right) \mu_i \quad (18)$$

where  $M_{ij}$  is defined as

$$M_{ij} = \sqrt{(2m_{ij}/m_i)} [\bar{\Omega}_{ij}^{(2,2)} / \bar{\Omega}_{ii}^{(2,2)}] \quad (19)$$

and the pure species viscosity is

$$\mu_i = \frac{1}{2} m_i n_i c_i l_i \quad (20)$$

where  $l_i$  is the mean free path, and  $\bar{\Omega}_{ij}$  is the energy-averaged collision integral for interaction between species  $i$  and  $j$ .

The translational contribution to the heavy species thermal conductivity is calculated using an equation similar to Eq. (18), with the pure species conductivity given as

$$\lambda_i = \frac{15}{8} k_b n_i c_i l_i \left( \frac{9\gamma_i - 5}{15\gamma_i - 15} \right) \quad (21)$$

The electron thermal conductivity is

$$\lambda_e = \left[ \frac{15}{8} k_b n_e^2 c_e l_e \left( \frac{9\gamma_e - 5}{15\gamma_e - 15} \right) \right] / \sum_{j=1}^N n_j M_{ij} \quad (22)$$

and electrical conductivity is calculated from

$$\sigma = n_e e^2 / m_e \sum_{i \neq e} n_i c_i \bar{\Omega}_{e-i}^{(1,1)} \quad (23)$$

The coefficients  $D_i$  are mixture-averaged according to

$$D_i = (1 - x_i) / \sum_{j \neq i} x_j / D_{ij} \quad (24)$$

where the  $D_{ij}$  are the binary mixture diffusion coefficients<sup>34</sup>:

$$D_{ij} = \frac{3}{16n\bar{\Omega}_{ij}^{(1,1)}} \left[ \frac{2k_b T(m_i + m_j)}{\pi m_i m_j} \right]^{1/2} \quad (25)$$

The electron and ion diffusion coefficients are modified to account for the ambipolar electric field. Assuming  $\nabla(n_e/\rho)/n_e \approx \nabla(n_{H^+}/\rho)/n_{H^+} \approx \nabla(n_{N^+}/\rho)/n_{N^+}$ , the ambipolar diffusion coefficients for electrons  $H^+$ , and  $N^+$  are

$$D_{a,e} = \frac{D_e(\mu_{H^+} n_{H^+} + \mu_{N^+} n_{N^+}) + \mu_e(D_{H^+} n_{H^+} + D_{N^+} n_{N^+})}{\mu_e n_e + \mu_{H^+} n_{H^+} + \mu_{N^+} n_{N^+}} \quad (26)$$

$$D_{a,H^+} = \frac{D_{H^+}(\mu_e n_e + \mu_{N^+} n_{N^+}) + \mu_{H^+}(D_e n_e - D_{N^+} n_{N^+})}{\mu_e n_e + \mu_{H^+} n_{H^+} + \mu_{N^+} n_{N^+}} \quad (27)$$

$$D_{a,N^+} = \frac{D_{N^+}(\mu_e n_e + \mu_{H^+} n_{H^+}) + \mu_{N^+}(D_e n_e - D_{H^+} n_{H^+})}{\mu_e n_e + \mu_{H^+} n_{H^+} + \mu_{N^+} n_{N^+}} \quad (28)$$

where the mobilities  $\mu$  are calculated from  $\mu_i = eD_i/k_b T_i$ .

The previous relations require the energy-averaged collision integrals for 28 species interactions. Collision integrals and collision cross sections are obtained from Refs. 35–41. Temperature-dependent curve fits are used for the transport property and elastic transfer calculations.

### Boundary Conditions

The physical boundary conditions for the continuity, momentum, energy, and electromagnetic equations are summarized in Table 2 and Fig. 1. At the inflow boundary 1A, the radial velocity is  $v = 0$ , and  $T$  and  $p$  are specified. The total pressure is adjusted to obtain the desired mass flow rate. The  $u$  velocities and the inlet static temperatures are then computed from the isentropic stagnation property relations. The effects of flow swirl are incorporated by specifying the azimuthal inlet  $w$  velocities as a fraction of the  $u$  velocities. At the solid cathode 1C and anode 1D surfaces, no-slip conditions are employed. Zero radial gradients are specified on the centerline 1E.

At the outflow boundary 1B, the static pressure is extrapolated from the interior of the flow. This is reasonable since the

Table 2 Boundary conditions for the fluid dynamic, energy, and electromagnetic equations<sup>a</sup>

Variable	Flowfield domain				
	1A	1B	1C	1D	1E
$u$	From stagnation properties	From momentum	0	0	$\frac{\partial u}{\partial r} = 0$
$v$	0	Extrapolated	0	0	0
$w$	Specified	Extrapolated	0	0	0
$T_e$	$\frac{\partial T_e}{\partial x} = 0$	Extrapolated	$\frac{\partial T_e}{\partial r} = 0$	$\frac{\partial T_e}{\partial r} = 0$	$\frac{\partial T_e}{\partial r} = 0$
$T_g$	From $M$ and $T_i$	Extrapolated	Specified $T_g(x)$	$T_g = T_a$	$\frac{\partial T_g}{\partial r} = 0$
$P$	Extrapolated	Extrapolated	$\frac{\partial P}{\partial n} = 0$	$\frac{\partial P}{\partial n} = 0$	$\frac{\partial P}{\partial r} = 0$
$V$	$\frac{\partial V}{\partial x} = 0$	$\frac{\partial V}{\partial x} = 0$	$V = V_{cat}$	$V_s = 13 \text{ V}$	$\frac{\partial V}{\partial r} = 0$
Variable	Anode domain				
	2A	2B	2C	2D	
$T_a$	$T_a = 1000 \text{ K}$	$\dot{q} = \epsilon \sigma (T_s^4 - T_{bg}^4)$	$\dot{q} = \lambda_h \frac{\partial T_g}{\partial \bar{n}} +  j  \left( V_s + \frac{5}{2e} k_b T_e \right) + \sum_{i=1}^N \frac{1}{m_i} \rho (C_{pi} T_i + h_i^0) D_i \frac{\partial y_i}{\partial \bar{n}} - \epsilon \sin \alpha \sigma (T_s^4 - T_{bg}^4)$	$\dot{q} = \epsilon \sigma (T_s^4 - T_{bg}^4)$	

<sup>a</sup>Energy equation boundary conditions are shown for both the fluid and anode domains. For radiative boundary conditions,  $T_s$  is the local anode surface temperature.

solutions indicate supersonic flow over the majority of the exit plane, with the subsonic region being confined to a thin annular region near the nozzle wall. The outflow  $u$  velocities are updated to satisfy continuity using velocity corrections as given by discretized forms of the momentum and continuity equations for the exit plane. This is consistent with the numerical solution method discussed later. A zero radial electron temperature gradient is employed at the walls 1C and 1D, effectively insulating the electrons from the solid surfaces.<sup>42</sup> This provides more physically accurate transport coefficient estimates, based on elevated electron temperatures and ionization levels, at the plasma/anode interface.

The boundary conditions for the voltage are shown in Table 2. The anode is modeled as an equipotential surface, whereas the cathode voltage is equipotential with the voltage updated to obtain the specified  $I$ . The axial gradient of the voltage is set to zero at the inflow and outflow boundaries so that current is forced to attach within the arcjet nozzle.

The assumption of plasma quasineutrality is not valid very near the electrode surfaces. The thickness of this sheath region is of the order of the Debye length, which is typically much smaller than the characteristic lengths for temperature and velocity changes. Net space charge creates electric fields in this region, which are large compared to those in the bulk plasma. Therefore, large voltage drops and power losses may occur. In this study, the electric fields in the sheath regions are treated as a fixed boundary condition, with an assumed anode sheath voltage fall of  $V_s = 13.0$  V. This value, chosen based on cathode fall voltage estimates for high-pressure arcs and estimates for the anode fall voltage from simple collisionless sheath theory,<sup>27</sup> is generally conservative in terms of the anode thermal loading.

The boundary conditions for the anode energy equation are also shown in Table 2. On the outer surfaces 2B and 2D, the local heat flux is given by radiation to the surroundings at a specified background temperature  $T_{bg} \ll T_a$  and a constant emissivity of  $\epsilon = 0.31$  for the tungsten anode.<sup>12</sup> Along the anode surface 2C, the net heat flux is a balance between 1) conduction and species diffusion heat fluxes to and from the flowfield, 2) the anode surface radiation loss through the exit plane to the surroundings, 3) the sheath losses given by the product of the local current density and an assumed sheath voltage drop  $V_s = 13$  V, and 4) the electron current enthalpy flux. Numerical solutions indicate that the optically thin plasma radiation loss term is less than 1% of the total electrical power input; therefore, radiation exchange between the plasma volume and the anode surface is neglected in this formulation. The upstream anode surface 2A is either a fixed temperature or zero heat flux boundary.

### Numerical Solution Method

The solution method is structured around the global continuity and momentum equations. These are solved using a compressible form of the pressure-based pressure-implicit with splitting of operators (PISO) algorithm,<sup>43</sup> where the density variations are implicitly included in the pressure-correction procedure as described by Rhie.<sup>44</sup> Staggered velocity and scalar grids yield a well-connected pressure field. Upstream weighted densities are employed to ensure numerical stability.<sup>45</sup> The governing equations are transformed into natural coordinates and solved on a uniform computational mesh. The equations are discretized over finite cell volumes, and power-law differencing of convective and diffusive portions of the linearized coefficients preserves numerical stability in regions of the flow where convection dominates. The solution process is iterative, and values for the field variables from the latest iteration are used to linearize the source terms. Underrelaxation is employed so that updated solutions are fractionally added to the solution from the previous iteration.

The energy equations are solved to update the temperature fields for the heavy species, electrons, and anode. The species

number densities, transport coefficients, and source terms are then updated using the latest available temperatures and pressures. The continuity and momentum equations are solved to update the pressure and velocity fields. Finally, the voltage and current density distributions are updated. Iterations are continued until 1) the normalized energy equation residuals are within 1% of the electrical power input, 2) the difference between the inlet and exit plane mass flow rates is less than 1% of the total mass flow rate, and 3) the axial and radial momentum equation residuals are within 1% of their respective exit momentum fluxes. Further details of the solution methodology can be found in Ref. 27.

### Results and Discussion

Results are presented for the geometry of a NASA Lewis Research Center 1-kW arcjet operating on simulated hydrazine ( $x_{mol} = 0.5$ ).<sup>46</sup> The arcjet constrictor is  $x = 0.25$  mm long with a diameter of  $d = 0.62$  mm. The nozzle has a half-angle of 20 deg and an area ratio of 225:1. The cathode gap spacing, as measured axially from the converging portion of the anode surface, is  $x = 0.58$  mm. The upstream anode surface 2A temperature (Fig. 1) is constant at  $T_a = 1000$  K, which is consistent with infrared pyrometry measurements of the exterior anode surface. The cathode 1C temperature varies linearly from  $T_c = 1000$  K at the inlet to the tungsten melting temperature of  $T_c = 3680$  K at the cathode tip. The choice for  $T_c$  agrees reasonably with experimental estimates based on emission spectroscopy measurements<sup>47</sup> and posttest observations that indicate the presence of a molten crater at the tip.<sup>46</sup> The inlet flow swirl velocity is 30% of the axial inflow velocity, and the inlet total temperature is  $T_t = 1000$  K.

The computational grids, shown in Fig. 2, are comprised of 62 axial by 27 radial nodes for the plasma, and 62 axial by 9 radial nodes for the anode domain. Numerical accuracy was investigated by examining the solutions for several of the field variables on both coarse and fine grids. Studies of the temperatures, axial velocity, and electron number density fields indicate typical fractional error estimates of roughly 5% based on Richardson extrapolation.<sup>48</sup> The fractional error estimate for the voltage is 3%. Simulation run time for the  $62 \times 27$  grid is roughly 20 hours on a Convex C240 mainframe computer.

The global performance parameters for the simulation are summarized as follows: propellant,  $N_2H_4$ ; mass flow rate, 44 mg/s; arc current, 10 A; terminal voltage, 101 V; thrust, 0.20 N; specific impulse, 459 s; and thrust efficiency, 0.45. The propellant is hydrazine operating at  $\dot{m} = 44$  mg/s and  $I = 10$  A. The predicted voltage is  $V = 101$  V, and the specific impulse is  $I_{sp} = 459$  s. The voltage prediction is somewhat lower than experimental measurements, whereas the  $I_{sp}$  and efficiency predictions are higher. Curran and Haag<sup>46</sup> measured  $V \approx 115$  V

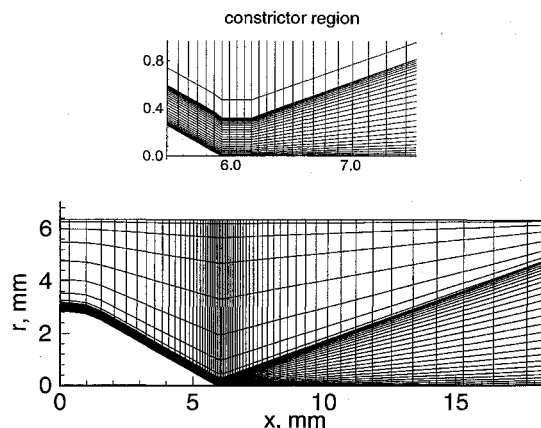


Fig. 2 Computational grids; the grids are tuned axially for high density in the constrictor and radially for high density near the electrode surfaces.

and  $I_{sp} \approx 435$  s at  $\dot{m} = 45.5$  mg/s and  $I = 10$  A. The underprediction in voltage may be because of neglect of the electron pressure gradient term in Ohm's law, and to deficiencies in modeling the cathode erosion, electrode sheath physics, and the inelastic energy exchange between the electrons and heavy species.

Contours of current density and anode temperature are indicated in Fig. 3. In the constrictor, the current is conducted in a region of  $\sim 100$ - $\mu$ m-diam, resulting in a centerline current density of  $j \approx 70,000$  A/cm<sup>2</sup>. The peak self-induced magnetic field is  $B_\theta \approx 0.04$  T, justifying the assumed neglect of the magnetic pressure compared to the gasdynamic pressure.

Further downstream, the arc becomes more diffuse and attaches to the nozzle wall. A peak anode attachment current density of  $j \approx 26$  A/cm<sup>2</sup> is noted at a location of  $x \approx 10$  mm, or roughly 4 mm downstream of the constrictor. The anode temperature increases from the upstream boundary value of  $T_a = 1,000$  K to  $T_a \approx 1,400$  K near the exit plane. Approximately 470 W of power is transferred from the plasma to the anode, primarily because of sheath and thermal conduction losses. This is roughly 38% of the sum of the electrical power input ( $P = 1010$  W) and the upstream boundary inflow enthalpy (215 W).

Heavy species and electron temperature contours in the constrictor region are shown in Figs. 4 and 5. In Fig. 4, a maximum of  $T_g \approx 21,000$  K occurs near the center of the constrictor. In the constrictor, the central region of the arc is near thermal equilibrium, as indicated by a similar maximum of  $T_e \approx 22,000$  K shown in Fig. 5. The outer region of the flow exhibits a high degree of thermal nonequilibrium, caused by intense ohmic heating of the electrons. This is shown in Fig. 5, where, at an axial location of  $x \approx 7.5$  mm, the electron temperature decreases radially from a centerline value of  $T_e \approx$

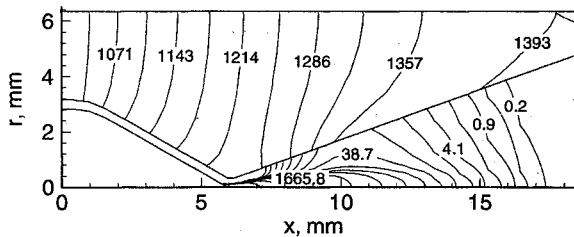


Fig. 3 Anode temperature and current density for hydrazine. The maximum anode current density is  $j \approx 26$  A/cm<sup>2</sup> at  $x \approx 10$  mm. The anode temperature increases from  $T_a \approx 1000$  K at the upstream surface to  $T_a \approx 1400$  K near the exit plane.

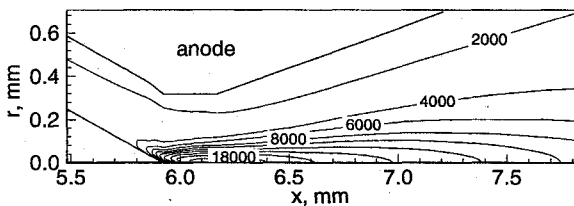


Fig. 4  $T_g$  contours in the constrictor region. The maximum is  $T_g \approx 21,000$  K at the constrictor centerline. The exit plane is located at  $x = 18.4$  mm.

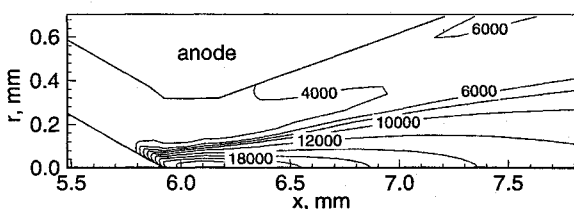


Fig. 5  $T_e$  contours in the constrictor region. The maximum is  $T_e \approx 22,000$  K at the constrictor centerline. The exit plane is located at  $x = 18.4$  mm.

13,000 K, eventually reaching a minimum of  $T_e \approx 6000$  K near the anode surface. From Figs. 3 and 4, the anode and heavy species temperatures are  $T_a \approx T_g \approx 1300$  K in this region, which indicates a temperature ratio of  $T_e/T_g \approx 4.5$ . The thermal nonequilibrium is more pronounced further downstream at the anode current attachment location ( $x \approx 10$  mm), where predictions indicate  $T_e/T_g \approx 6$ , or an electron temperature of  $T_e \approx 8000$  K. The thermal nonequilibrium indicated near the anode is qualitatively similar to the predictions of other nonequilibrium hydrogen arcjet models.<sup>16,17</sup> The locally elevated electron temperatures enhance ionization levels and allow current conduction through the cold gas layer near the nozzle wall.

Axial velocity contours are shown in Fig. 6. A maximum centerline velocity of  $u \approx 11$  km/s occurs at  $x = 7$  mm, compared to a lower velocity near the constrictor exit because of intense arc heating. The velocity at the exit plane is  $u \approx 6.5$  km/s. Although the centerline flow velocity decreases, the nozzle produces axial acceleration over the entire length in the cooler outer flow region. The arc displaces the majority of the mass and momentum fluxes toward this outer region, because of the high radial gradients in heavy species temperature. The nozzle performance is largely determined by the acceleration of the high mass density outer flow region, rather than the deceleration of the low-density, high-temperature central flow. This suggests that performance benefits would be available from higher area ratio nozzles.

Model predictions are compared with experimental temperature measurements in Fig. 7. Nozzle centerline predictions for electron  $T_e$  and heavy species  $T_g$  temperatures are compared with internal nozzle emission spectroscopy measurements of excitational, vibrational, and rotational temperature.<sup>49</sup> Electrostatic probe measurements for electron and ion translational temperatures downstream of the exit plane ( $x = 18.4$  mm) are also indicated.<sup>50</sup> Model predictions for  $T_g$  are in good agreement with the N<sub>2</sub> vibrational and rotational temperature measurements, indicating that these temperatures may be roughly in equilibrium with the heavy species translational temperatures. The exit plane prediction of  $T_g \approx 2500$  K also agrees well with the plume measurements for ion temperature. The agreement between  $T_e$  and the H-atom excitation and electron temperature is less favorable, as the model underpredicts the

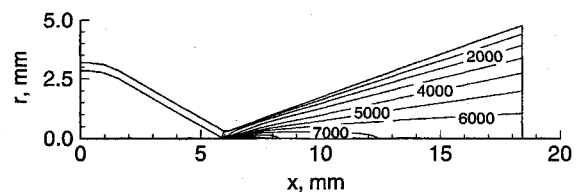


Fig. 6 Axial  $u$  velocity contours. The maximum is  $u \approx 11$  km/s at  $x \approx 7$  mm. The centerline velocity decreases to  $u \approx 6.5$  km/s at the exit plane.

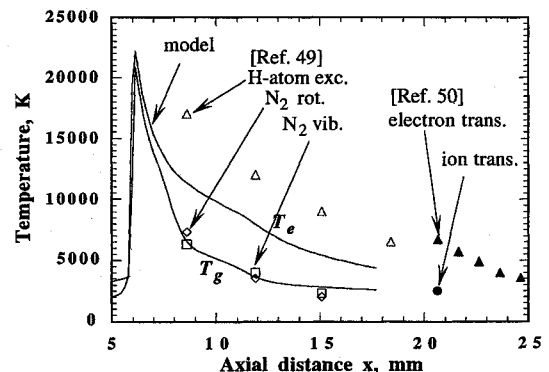


Fig. 7 Comparison of  $T_e$  and  $T_g$  temperature predictions with experimental measurements.<sup>49,50</sup>

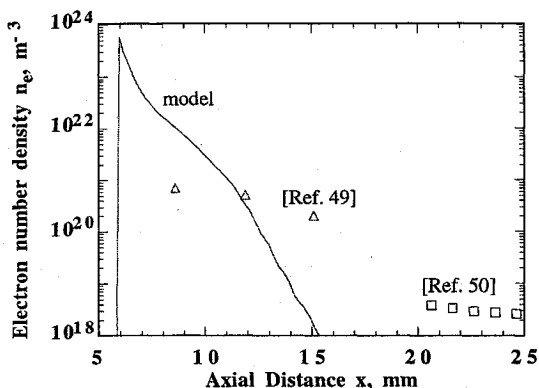


Fig. 8 Comparison of centerline  $n_e$  predictions with experimental measurements.<sup>49,50</sup>

data by roughly 50%. Despite this discrepancy, the agreement between the experimentally observed and predicted trends for thermal nonequilibrium clearly illustrates the need for at least two energy equations to model the arcjet plasma flowfield accurately.

Centerline predictions for  $n_e$  are compared with the experiment in Fig. 8.<sup>49,50</sup> In the upstream portion of the flow, at  $x \approx 8.5$  mm, the model predicts  $n_e \approx 1 \times 10^{22} \text{ m}^{-3}$ , which is approximately 1 order of magnitude greater than the experimental estimate, while downstream, at  $x \approx 15$  mm, the predicted density of  $n_e \approx 1 \times 10^{18} \text{ m}^{-3}$  is roughly two orders of magnitude lower than experiment. It is likely that the recombination of electrons is limited by finite rate chemistry, and chemical nonequilibrium models are required to capture the species distributions more accurately.

### Summary and Conclusions

A two-temperature chemical equilibrium model is formulated for  $\text{N}_2/\text{H}_2$  arcjets. In this approach, a modified set of Navier–Stokes equations is employed, with separate energy equations to determine electron and heavy species temperatures. The species number densities are calculated using relations derived from the law of mass action, the plasma equation of state, charge neutrality, and species conservation.

Results for the 1-kW NASA Lewis Research Center thruster indicated a high degree of thermal nonequilibrium in the voltage fall region near the nozzle wall, with  $T_e/T_g \approx 6$  predicted at the location of maximum anode current density. This nonequilibrium is a primary mechanism for maintaining the ionization levels required for electrical conduction through the cool near-electrode regions of the flow.

The model was compared with experimental measurements. Centerline heavy species temperature predictions agree favorably with measurements of  $\text{N}_2$  rotational and vibrational temperatures, and estimates for the translational ion temperature in the near plume. Centerline electron temperature predictions, while in qualitative agreement with experiment, are roughly 50% lower than experimental measurements for H-atom excitation and electron translational temperature measurements. Also, significant discrepancies are noted between predicted and measured centerline electron number densities. The model must be generalized to chemical nonequilibrium to 1) capture the competing effects of finite rate chemical kinetics, convection, and mass diffusion and 2) accurately describe the inelastic energy exchange rates between the electrons and heavy species. This may resolve discrepancies between the model predictions and experimental measurements of electron concentrations and temperatures.

### Acknowledgments

This work is funded by the U.S. Air Force Office of Scientific Research under Contracts F49620-92-J-0448 and -0280.

Mitat Birkan is the Program Manager. The authors wish to acknowledge stimulating dialogues with S. Bufton, N. Tiliakos, and G. Willmes. We thank S. P. Vanka and K. Cope for their advice on solving the energy equation in strong conservative form, M. J. Kushner for helpful advice in constructing the model, and M. Martinez-Sanchez for helpful discussions regarding the Saha equation. We also thank J. Lu for assistance with the simulations and preparation of figures.

### References

- Wilbur, P. J., Jahn, R. G., and Curran, F. C., "Space Electric Propulsion Plasmas," *IEEE Transactions on Plasma Science*, Vol. 19, No. 6, 1991, pp. 1167–1179.
- Butler, G. W., Cassady, R. J., and King, D. Q., "Directions for Arcjet Technology Development," AIAA Paper 94-2652, June 1994.
- Jack, J. R., "Theoretical Performance of Propellants Suitable for Electrothermal Jet Engines," *ARS Journal*, Vol. 31, No. 12, 1961, pp. 1685–1689.
- John, R. R., Bennett, S., Coss, L. A., Chen, M. M., and Connors, J. F., "Energy Addition and Loss Mechanisms in the Thermal Arcjet Engine," AIAA Paper 63-022, March 1963.
- Topham, D. R., "The Electric Arc in a Constant Pressure Axial Gas Flow," *Journal of Physics D: Applied Physics*, Vol. 4, No. 8, 1971, pp. 1114–1125.
- Glockner, B., Schrade, H. O., and Auweter-Kurtz, M., "Performance Calculation of Arcjet Thrusters: The Three Channel Model," International Electric Propulsion Conf., Paper 93-187, Sept. 1993.
- Martinez-Sanchez, M., and Sakamoto, A., "Simplified Analysis of Arcjet Thrusters," AIAA Paper 93-1904, June 1993.
- Martinez-Sanchez, M., "Arcjet Modeling: Status and Prospects," AIAA Paper 94-2653, June 1994.
- Butler, G. W., Kashiwa, B. A., and King, D. Q., "Numerical Modeling of Arcjet Performance," AIAA Paper 90-1474, June 1990.
- Butler, G. W., and King, D. Q., "Single and Two Fluid Simulations of Arcjet Performance," AIAA Paper 92-3104, July 1992.
- Butler, G. W., Kull, A. E., and King, D. Q., "Numerical Simulations of Hydrogen Arcjet Performance," International Electric Propulsion Conf., Paper 93-249, 1993.
- Butler, G. W., Kull, A. E., and King, D. Q., "Single Fluid Simulations of Low Power Hydrogen Arcjets," AIAA Paper 94-2870, June 1994.
- Rhodes, R., and Keefer, D., "Numerical Modeling of an Arcjet Thruster," AIAA Paper 90-2614, June 1990.
- Rhodes, R., and Keefer, D., "Modeling Arcjet Space Thrusters," AIAA Paper 91-1994, June 1991.
- Rhodes, R., and Keefer, D., "Non-Equilibrium Modeling of Hydrogen Arcjet Thrusters," International Electric Propulsion Conf., Paper 93-217, Sept. 1993.
- Miller, S., and Martinez-Sanchez, M., "Two Fluid Nonequilibrium Simulation of Hydrogen Arcjet Thrusters," *Journal of Propulsion and Power*, Vol. 12, No. 1, 1996, pp. 112–119.
- Keefer, D., Burtner, D., Moeller, T., and Rhodes, R., "Multiplexed Laser Induced Fluorescence and Non-Equilibrium Processes in Arcjets," AIAA Paper 94-2656, June 1994.
- Flowe, A. C., DeWitt, K. J., Keith, T. G., Jr., Pawlas, G. E., and Penko, P. F., "Numerical Modeling of Fluid and Electromagnetic Phenomena in an Arcjet," AIAA Paper 92-3106, July 1992.
- Ciucci, A., d'Agostino, L., and Andrenucci, M., "Development of a Numerical Model of the Nozzle Flow in Low Power Arcjet Thrusters," International Electric Propulsion Conf., Paper 93-182, Sept. 1993.
- Fujita, K., and Arakawa, Y., "Anode Heat Loss and Current Distributions of DC Arcjets," International Electric Propulsion Conf., Paper 93-185, June 1993.
- Babu, V., Aithal, S., and Subramaniam, V. V., "On the Effects of Swirl in Arcjet Thruster Flows," International Electric Propulsion Conf., Paper 93-183, Sept. 1993.
- Babu, V., Aithal, S., and Subramaniam, V. V., "Vibrational Non-Equilibrium in Arcjet Flows," International Electric Propulsion Conf., Paper 93-129, Sept. 1993.
- Kruger, C. H., and Mitchner, M., "Kinetic Theory of Two Temperature Plasmas," *Physics of Fluids*, Vol. 10, No. 9, 1967, pp. 1953–1961.
- Mertogul, A. E., "Modeling and Experimental Measurements of Laser Sustained Plasmas," Ph.D. Dissertation, Dept. of Mechanical and Industrial Engineering, Univ. of Illinois, Urbana, IL, 1993.
- Sutton, G. W., and Sherman, A., *Engineering Magneto-Hydrodynamics*, McGraw-Hill, New York, 1965, pp. 148–190.

- <sup>26</sup>Megli, T. W., Krier, H., and Burton, R. L., "Plasmadynamics Model for Nonequilibrium Processes in  $N_2/H_2$  Arcjets," *Journal of Thermophysics and Heat Transfer*, Vol. 10, No. 4, 1996, pp. 554–562.
- <sup>27</sup>Megli, T. W., "A Nonequilibrium Plasmadynamics Model for Nitrogen/Hydrogen Arcjets," Ph.D. Dissertation, Dept. of Mechanical and Industrial Engineering, Univ. of Illinois, Urbana, IL, 1995.
- <sup>28</sup>Incropera, F. P., and Dewitt, D. P., *Fundamentals of Heat and Mass Transfer*, Wiley, New York, 1981, p. 758.
- <sup>29</sup>Van de Sanden, M. C. M., Schram, P. P. J. M., Peeters, A. G., Van der Mullen, J. A. M., and Kroesen, G. M. W., "Thermodynamic Generalization of the Saha Equation for a Two-Temperature Plasma," *Physical Review A: General Physics*, Vol. 40, No. 9, 1989, pp. 5273–5276.
- <sup>30</sup>Eddy, T. L., Leger, J. M., and Coudert, F. P., "Nonequilibrium Diagnostics of a Nitrogen Plasma Jet," *Heat Transfer in Thermal Processing*, American Society of Mechanical Engineers, HTD-Vol. 161, New York, 1991.
- <sup>31</sup>Fan, W. X., and Dudeck, M. A., "A Study of Concentrations in a Nitrogen Plasma Under Thermal Unbalance Conditions," *Journal of Chemical Physics*, Vol. 88, No. 1, 1991, pp. 27–37.
- <sup>32</sup>Drellishak, K. S., "Partition Functions and Thermodynamic Properties of High Temperature Gases," Ph.D. Dissertation, Northwestern Univ., Evanston, IL, 1963.
- <sup>33</sup>Mitchner, M., and Kruger, C., *Partially Ionized Gases*, Wiley, New York, 1973.
- <sup>34</sup>Maitland, G. C., Rigby, M., Smith, B. E., and Wakeham, W. A., *Intermolecular Forces*, Clarendon, Oxford, England, UK, 1981, p. 302.
- <sup>35</sup>Capecchi, G., and d'Agostino, L., "Numerical Model of Equilibrium Composition and Transport Coefficients of Hydrazine Under Dissociation and Ionization," AIAA Paper 94-2868, June 1994.
- <sup>36</sup>Stallcop, J. R., Partridge, H., and Levin, E., "Resonance Charge Transfer, Transport Cross Sections, and Collision Integrals for  $N^+(3P)-N(^4S)$  and  $O^+(^4S)-O(^3P)$  Interactions," *Journal of Chemical Physics*, Vol. 95, No. 9, 1991, pp. 6429–6439.
- <sup>37</sup>Stallcop, J. R., Bauschlicher, C. W., Partridge, H., and Levin, E., "Theoretical Study of Hydrogen and Nitrogen Interactions: N-H Transport Cross Sections and Collision Integrals," *Journal of Chemical Physics*, Vol. 97, No. 8, 1992, pp. 5578–5585.
- <sup>38</sup>Levin, E., Partridge, H., and Stallcop, J. R., "Collision Integrals and High Temperature Transport Properties for N-N, O-O, and N-O," *Journal of Thermophysics and Heat Transfer*, Vol. 4, No. 4, 1990, pp. 469–477.
- <sup>39</sup>Vanderslice, J. T., Weissman S., Mason, E. A., and Fallon, R. J., "High Temperature Transport Properties of Dissociating Hydrogen," *Physics of Fluids*, Vol. 5, No. 2, 1962, pp. 155–164.
- <sup>40</sup>Stallcop, J. R., Partridge, H., Walch, S. P., and Levin, E., "H-N<sub>2</sub> Interaction Energies, Transport Cross Sections, and Collision Integrals," *Journal of Chemical Physics*, Vol. 97, No. 5, 1992, pp. 3431–3436.
- <sup>41</sup>Grier, N. T., "Calculation of Transport Properties of Ionizing Atomic Hydrogen," NASA TN D-1386, April 1966.
- <sup>42</sup>Chang, C. H., and Pfender, E., "Nonequilibrium Modeling of Low Pressure Argon Plasma Jets; Part I: Laminar Flow," *Plasma Chemistry and Plasma Processing*, Vol. 10, No. 3, 1990, pp. 473–491.
- <sup>43</sup>Issa, R. I., "Solution of the Implicitly Discretised Fluid Flow Equations by Operator-Splitting," *Journal of Computational Physics*, Vol. 62, No. 1, 1986, pp. 40–65.
- <sup>44</sup>Rhie, C. M., "A Pressure-Based Navier-Stokes Solver Using the Multigrid Method," AIAA Paper 86-0207, Jan. 1986.
- <sup>45</sup>Karki, K. C., "A Calculation Procedure for Viscous Flows at All Speeds in Complex Geometries," Ph.D. Dissertation, Univ. of Minnesota, Minneapolis, MN, 1986.
- <sup>46</sup>Curran, F. M., and Haag, T. W., "Extended Life and Performance Test of a Low-Power Arcjet," *Journal of Spacecraft and Rockets*, Vol. 29, No. 4, 1992, pp. 444–452.
- <sup>47</sup>Cappelli, M. A., and Storm, P. V., "Interior Plasma Diagnostics of Arcjet Thrusters," AIAA Paper 94-2654, June 1994.
- <sup>48</sup>Roache, P. J., "A Method for Uniform Reporting of Grid Refinement Studies," *Symposium on Quantification of Uncertainty in Computational Fluid Dynamics* (Washington, DC), American Society of Mechanical Engineers, New York, 1993.
- <sup>49</sup>Zube, D. M., and Myers, R. M., "Thermal Nonequilibrium in a Low-Power Arcjet Nozzle," *Journal of Propulsion and Power*, Vol. 9, No. 4, 1993, pp. 545–552.
- <sup>50</sup>Buften, S. A., Burton, R. L., and Krier, H., "Measured Plasma Properties at the Exit Plane of a 1 kW Arcjet," AIAA Paper 95-3066, July 1995.